Supplementary Information (SI) for Chemical Science.
This journal is © The Royal Society of Chemistry 2024

Supplementary Information for "The induction effect does not explain electron density in haloacetates: Are our textbooks wrong?"

Edwin C. Johnson*[1,2], Kasimir P. Gregory[2,3,4,5], Hayden Robertson[2,6], Isaac J. Gresham[7,8], Andrew R. J. Nelson[9], Vince S. J. Craig[3], Stuart W. Prescott[7], Alister J. Page[2], Grant B. Webber[2], and Erica J. Wanless[2]

[1]Department of Chemistry, University of Sheffield, UK
[2]College of Science, Engineering and Environment, University of Newcastle, Callaghan, NSW 2308, Australia
[3]Division of Biomedical Science and Biochemistry, Research School of Biology, The Australian National University, Canberra, ACT 0200, Australia
[4]Department of Materials Physics, Research School of Physics, The Australian National University, Canberra, ACT 0200, Australia
[5]School of Science and Technology, University of New England, Armidale, NSW 2351, Australia
[6]Soft Matter at Interfaces, Institute for Condensed Matter Physics, Technische Universität Darmstadt, 64289 Darmstadt, Germany
[7]School of Chemistry, University of Sydney, Sydney, NSW 2006, Australia
[8]School of Chemical Engineering, UNSW Sydney, NSW 2052, Australia
[9]ANSTO, Locked Bag 2001, Kirrawee DC, Australia
*email: *e.c.johnson@sheffield.ac.uk*

Contents

1 Experimental

1.1 Materials

Silicon wafers used for ellipsometry were purchased from Silicon Valley Microelectronics (USA). Silicon blocks (100 mm diameter, 10 mm thick) used for neutron reflectometry where purchased from El-Cat Inc. (USA). Sodium hydroxide (NaOH) was purchased from Chem-Supply. Surface fuctionalisation reagents (3-aminopropyl) triethoxysilane (APTES, >99%), 2-bromoisobutyrate bromide (BIBB, >99%), and triethylamine (TEA, 99%) were purchased from Sigma-Aldrich. Tetrahydrofuran (THF, >99%) was purchased from RCI Labscan Ltd and was dried over 4 Å molecular sieves prior to use. Methanol and ethanol (AR grade) were purchased from Sigma-Aldrich and used as received. Ethanol was used to clean the wafers/blocks. Methanol was used as a co-solvent for the polymerisation reaction. Polymerisation reagents copper bromide ($CuBr_2$, 99.999%), 2,2′-bipyridine (bipy, 99%), 1,1,4,7,10,10-hexamethyltriethylene-tetramine (HMTETA, 97%), and reducing agent (+)-sodium L-ascorbate (>98%) were purchased from Sigma-Aldrich and used as received. The following sodium salts were purchased from Sigma Aldrich and used as received: acetate (CH_3COO^-), trifluoro-acetate (CF_3COO^-), chlorodifluoroacetate ($CClF_2COO^-$), trichloroacetate (CCl_3COO^-). All glassware was washed thoroughly in a 10% HNO_3 acid bath for at least 24 h, followed by copious rinsing with Milli-Q water (Merck Millipore, 18.2 MΩ · cm at 25 °C). Milli-Q water was used throughout, excluding NR experiments which used D_2O. Halogenated acetic acid undergoes thermal decomposition. However neither the salt nor free acid decompose in water.[1] Poly(*N*-isopropylacrylamide) was purchased from Polysciences Inc. and used as received for all turbidity measurements.

1.2 Computational techniques

1.2.1 þ calculation

Lone ions were optimised with MP2/aug-cc-pVQZ using the Gaussian16[2] program and the alkyl halides with MP2/aug-cc-pVQZ using the ORCA 5.0[3] program. Partial charges and þ values of these optimised structures were then calculated via a Density Derived Electrostatic and Chemical (DDEC6) charge distribution analysis[4] using the approach described by Gregory et al.[5] This choice in computational methodology has been validated across multiple experimental results by Gregory et al.[5] The effect of changing the decomposition method, functional, and basis set on these halo-acetate oxygen partial charge trends is shown in Figure S1.

1.2.2 SAPT calculations

A detailed description of the methodology is described by Gregory et al. for amino-acid ion interactions.[6] Briefly, for each ion-solvent and ion-NIPAM fragment combination, 1000 unique starting geometries between the two species were generated with Packmol.[7] These underwent an initial optimisation using 3rd order density functional tight binding (DFTB3)[8] including D3(BJ) dispersion corrections[9] and the 3ob-3-1 parameter set[10] before unique geometries were reoptimised with M06-2X/aug-cc-pVDZ in the Gaussian16 program.[2] Symmetry Adapted Perturbation Theory[11–13] (SAPT) including electron correlation at the couple cluster singles doubles (CCSD) level for each monomer in

electrostatics and 3rd-order dispersion (SAPT2+3) [14–16] with an aug-cc-pVDZ basis set was used on each optimised ion-solvent and ion NIPAM fragment structure. SAPT2+3 calculations employed the superposition of atomic densities [17, 18] as an initial guess to calculate the electrostatic (elec), exchange(-repulsion) (exch), induction (ind), dispersion (disp) and total interaction energy contributions at the M06-2X/aug-cc-pVDZ optimised geometry. All SAPT calculations employed the Psi4 package.[19]

1.2.3 DFTB MD Simulations

Molecular Dynamics (MD) trajectories were calculated using the DFTB+ software package.[20] Initial geometries for all MD trajectories consisted of a single NIPAM fragment and a single cation-anion pair, and were solvated using PACKMOL.[7] MD simulations were performed using 3rd order density functional tight binding (DFTB3-D3(BJ)/3ob-3-1) energies and gradients, computed 'on the fly' at each MD timestep. Charge mixing was configured with the Broyden method.[21] All MD trajectories were performed using constant volume & temperature dynamics (i.e. NVT ensemble) via a Nosé-Hoover chain[22, 23] (NHC) thermostat (chain-length = 3) at 300 K with a coupling constant of 1000 cm^{-1}. Cubic periodic boundary conditions (PBC) were enforced on all trajectories, with charges handled via particle mesh Ewald summation. All MD trajectories were iterated using a timestep of 1 fs, with coordinates and relevant information recorded every 10 fs. MD trajectories are up to 500 −700 ps in length and the spatial distribution functions were calculated from a combined cube file from the 10 replicates of each anion subset using TRAVIS.[24]

1.3 Synthetic protocols

1.3.1 Grafting of PNIPAM chains via surface-initiated ARGET ATRP

Fuctionalisation of planar silicon wafers with ARGET ATRP initiator moieties was conducted using an experimental protocol we have previously reported.[25] Silicon (100) wafers were cut into small pieces ($\sim 1\times2.5$ cm^2) before being UV-ozone cleaned for 30 min using a Bioforce Nanosciences ProCleaner and rinsed in 10 wt% NaOH for 30 seconds. The treated wafers were dried and placed in an open petri dish along with a 3 mL glass vial containing ∼100 µL APTES. The petri dish was then placed in a desiccator, which was sealed and placed under vacuum. Vapour deposition was allowed to progress for 30 min before the wafers were removed and placed in an oven heated at 110 °C for 30 min. The wafers were then functionalised by immersion in THF followed by sequential addition of triethylamine (final concentration = 0.2 M) and BIBB (final concentration = 0.2 M), allowing the surface reaction to proceed for 1 h. Finally, the initiator-functionalised silicon wafers were rinsed extensively with ethanol and deionised water, before drying under a stream of compressed air.

Following surface functionalisation with ATRP initiator groups, surface-initiated ARGET ATRP was employed to graft PNIPAM brushes from each wafer.[25] Briefly, a molar ratio of 900:1.5:15:10 for PNIPAM:$CuBr_2$:HMTETA:AscA was used. 1:2 v/v methanol/water mixture was added with the final monomer-to-solvent mass ratio being 0.058/1. Each PNIPAM-coated silicon wafer was rinsed thoroughly with ethanol and deionised water before drying under a stream of N_2 gas. The kinetics of such surface-initiated polymerisations differ from those for the analogous solution polymerisations[26, 27] and the determination of molecular weight for the PNIPAM chains via brush degrafting is not feasible (owing to

the small mass of recovered polymer). Thus, the brush grafting density was assumed to be comparable to earlier brushes prepared using similar synthesis protocols.[25]

Table S1: Summary of PNIPAM dry brush thickness† for each brush investigated.

***In situ* measurement**	**Ellipsometrically determined dry brush thickness** [Å]	**NR determined dry brush thickness** [Å]	**Molecular weight** ‡ [g·mol^{-1}]
Ellipsometry	651 ± 2.0	-	580 000
NR	232.0 ± 2.9	246.7 ± 0.3	170 700

†Uncertainty in ellipsometry measurement comes from standard deviation across multiple measurements across the surface. Uncertainty in the value reported for neutron reflectometry thicknesses is the spread of acceptable thickness derived from the Markov chain Monte Carlo (MCMC) fitting.
‡Estimated using equation from Brittain[28] using previously reported grafting densities.[25]

1.4 Characterisation techniques

1.4.1 Cloud point measurements

Cloud point measurements were performed on a Shimadzu UV-1900i spectrophotometer with S-1700 Thermoelectric temperature controller to determine the LCST of ungrafted PNIPAM in various electrolytes of 100 mM, 250 mM and 500 mM. All PNIPAM samples were made to a polymer concentration of 0.1 wt% with MilliQ water. The reference cell contained pure MilliQ at all times. Absorption measurements were taken using a wavelength of 500 nm every 24 s whilst the temperature was increased from 20 °C to 45 °C at 0.5 °C/min. The LCST was then calculated by finding the half-height between the two plateau regions in the absorbance data.

1.4.2 Ellipsometry

Dry brush thickness for each brush was determined using a Nanofilm EP4 spectroscopic imaging ellipsometer using a single wavelength (658 nm). Measurements were made at five angles of incidence between 45° and 60°. Dry brush thicknesses are summarised in Table S1. Reported values are an average of multiple positions across the surface.

In situ aqueous ellipsometry measurements were conducted on a Nanofilm EP4 spectroscopic imaging ellipsometer. Measurements were conducted in a Nanofilm solid–liquid fluid cell with optical glass windows at 65°, mounted on a copper base plate with an integrated fluid heat exchanger. For spectroscopic measurements, ellipsometric parameters were measured at 12 evenly spaced wavelengths between 400 nm and 910 nm.

A protocol for *in situ* ellipsometry brush experiments, including initial hydration and establishment of reversible behaviour, is described in Robertson et al.[29] This protocol was adopted here for the four sodium salts examined.

Ellipsometry data was modelled with the *refellips* software package,[30] as we have previously described.[31] Here we employ a model analogous to our NR approach (described below) using a four-component NR model. The interfacial structure consisted of water (or air for dry measurements), polymer, silica, and silicon slabs, respectively, each describing the refractive index, thickness, and solvent volume fraction within the particular slab.

The hydrated brush thickness was then converted into a swelling ratio (SR) to normalise between samples of different dry brush thicknesses. The LCST of the PNIPAM brush in each condition was determined by fitting a sigmoid function to the brush thickness vs temperature data. The LCST was taken as the inflection point of the fitted sigmoid curve.

1.4.3 Neutron reflectometry

Specular neutron reflectometry measurements were conducted on the *Platypus* time-of-flight neutron reflectometer at the 20 MW OPAL reactor (ANSTO, Lucas Heights, Australia).[32] For dry measurements, reflectivity was collected at angles of incidence of 0.65° and 3.0°, yielding a Q-range of 0.008 Å^{-1} to 0.26 Å^{-1}. For *in situ* (solvated) measurements, a Q-range of 0.01 Å^{-1} to 0.30 Å^{-1} was achieved using angles of incidence of 0.9° and 3.5°. A constant 65 mm footprint was maintained throughout. Choppers 1 and 3 were used for all measurements and a constant $\mathrm{d}Q/Q$ resolution of 8% was maintained. A standard solid-liquid cell was used throughout, which was encased by two temperature jackets controlled by a Julabo FP50-HE heater/chiller unit. Previous reports demonstrate the suitability of this setup for polymer brushes.[29, 31, 33–35] All measurements characterising the structure of the brush were made in D_2O electrolytes and measurements probing changes in the interfacial volume of electrolyte within the brush were made in water contrast-matched to the SLD of PNIPAM ($0.8 \times 10^{-6}\text{Å}^{-2}$, 19.7 vol% D_2O, hence referred to as CM).[35] All *in situ* measurements were acquired in an upward reflecting geometry, with temperature ramped from cold to hot. Temperatures were chosen to capture the structure of the brush below ($T < 32.5\,°\text{C}$), at ($T = 32.5\,°\text{C}$) and above ($T > 32.5\,°\text{C}$) the reported LCST of PNIPAM in pure water.[33, 36] For all electrolytes at 40 °C, the reflectivity of the brush was only measured at 0.9° due to time constraints; however, this is more than sufficient to capture the collapsed profile of the brush. Before exposing the brush to a new electrolyte identity, the brush was flushed with at least 15 mL of pure D_2O at 15 °C.

All NR data were reduced and modelled using the *refnx* software package.[37] We have previously shown that in the presence of various alkanoate ions (e.g., acetate), PNIPAM exhibits a non-monotonic volume fraction (VF) profile.[31] Consistent with our previous investigations,[31] we employ an identical model herein for the behaviour of a PNIPAM brush in these halogenated acetate electrolytes. Briefly, the NR model consisted of two main components: uniform slabs and a freeform piecewise cubic Hermite interpolating polynomial (PCHIP). The slabs were employed to describe the solvent backing and the silicon fronting, as well as the native oxide layer and the proximal polymer layer. The 4-knot PCHIP delineated the diffuse nature of the brush. From fronting to backing, the model was comprised of silicon, silica, proximal polymer, diffuse polymer, and solvent. Further details on this model are explored by Robertson et al. and Gresham et al.[31, 34]

For the analysis of all CM measurements, the model was analogous to that of the D_2O electrolytes; from fronting to backing the model consisted of silicon, silica, proximal salt, and solvent slabs, with a freeform PCHIP describing the concentration gradient of salt placed prior to the solvent slab. The SLD of the solvent was permitted to vary between $0.75 \times 10^{-6}\text{Å}^{-2}$ to $0.85 \times 10^{-6}\text{Å}^{-2}$ (initial set point = $0.8 \times 10^{-6}\text{Å}^{-2}$). The SLD of each salt component was allowed to vary slightly around their calculated values, using molecular volumes obtained from DDEC6 computations on MP2/aug-cc-pVQZ optimised structures and wave function files. The ion VF profile was permitted to be non-monotonic and the

extent of the profile was bounded by the extent of the polymer VF profile in the respective D_2O condition.

For both D_2O and CM data sets, the objectives were initially optimised by multiple differential evolution iterations, followed by subsequent sampling of the posterior distribution function by parallel-tempered Markov chain Monte Carlo (PT-MCMC) simulations. All D_2O results presented represent the median fit from the PT-MCMC sampling. Results pertaining to the CM data set are taken as the median across all the samples. Errors are the corresponding standard deviation. The brush thickness was then deduced from the polymer VF profiles *via* twice the first moment:

$$L_{1\mathrm{st}} = \frac{\int_0^\infty z \cdot \phi(z)\,\mathrm{d}z}{\delta_{\mathrm{dry}}} \tag{S1}$$

The interfacial volume of salt was calculated as the area under the salt VF profile.

2 Comparison of charge densities from different decomposition methods

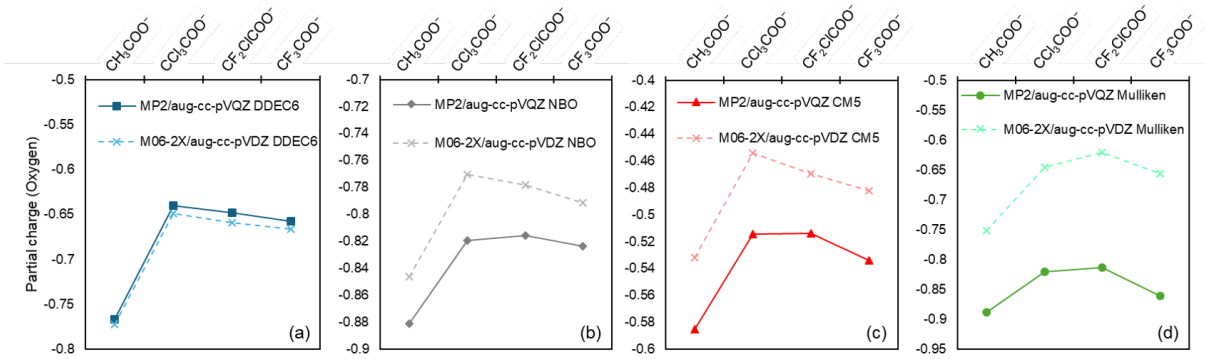

Figure S1: Partial charge of the O^- in substituted acetates determined by a number of decomposition methods: (a) DDEC6, (b) NBO, (c) CM5 and (d) Mulliken. DDEC6 is used in the main manuscript as it is the least susceptible to changes in the functional and basis set of these charge decomposition analysis techniques.[4]

3 Relationship between charge density and $\mathrm{p}K_\mathrm{a}$

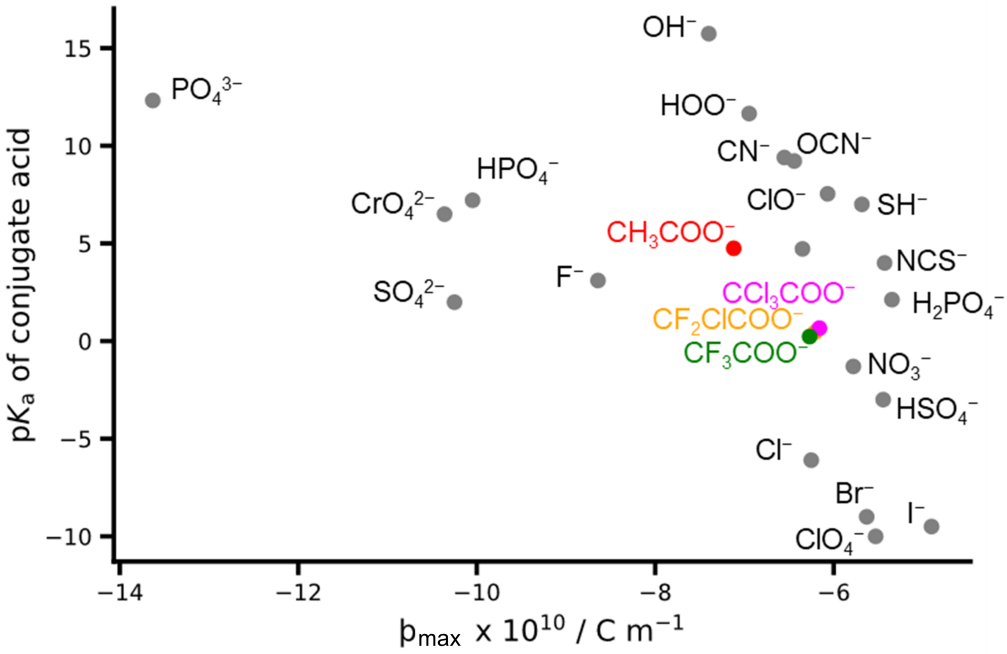

Figure S2: Charge density of a collection of monoatomic and polyatomic bases and the $\mathrm{p}K_\mathrm{a}$ values of their conjugate acids. Here, charge density is parameterised by þ_max, a parameter describing the site-specific radial charge density for ions.[5] þ_max denotes the greatest charge density within a polyatomic ion.

4 *In situ* ellipsometry

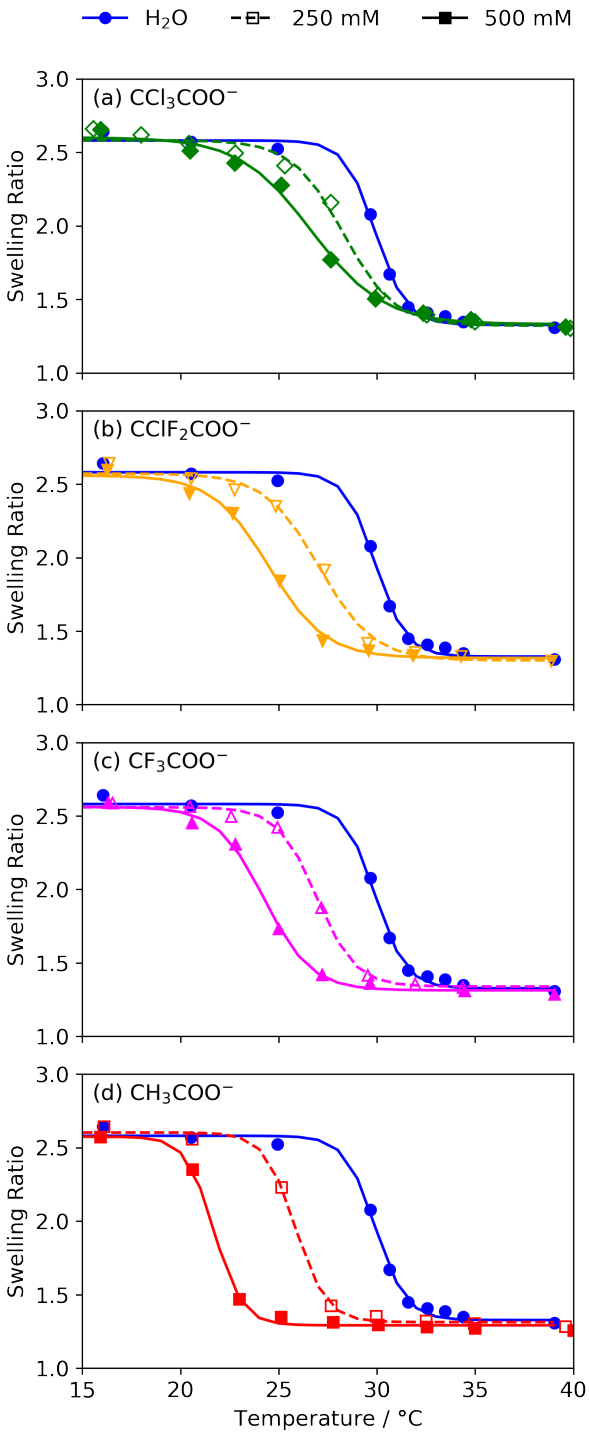

Figure S3: Ellipsometrically determined PNIPAM brush swelling ratio as a function of temperature in aqueous electrolytes of (substituted) acetates. Solid or dashed lines are sigmoidal fits through data. The inflection point of these curves was used as the extract LCST values.

5 Oxygen partial charge and charge density relationship

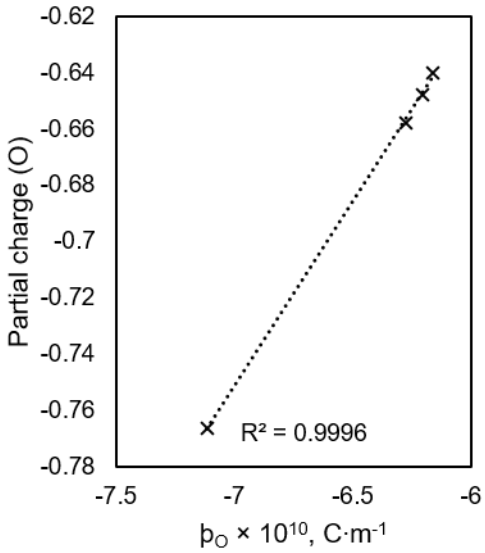

Figure S4: O^- partial charge against $þ_{O^-}$ for the investigated acetate series. There is a clear linear relationship between the partial charge on the oxygen and its radial charge density.

6 Symmetry adapted perturbation theory calculations

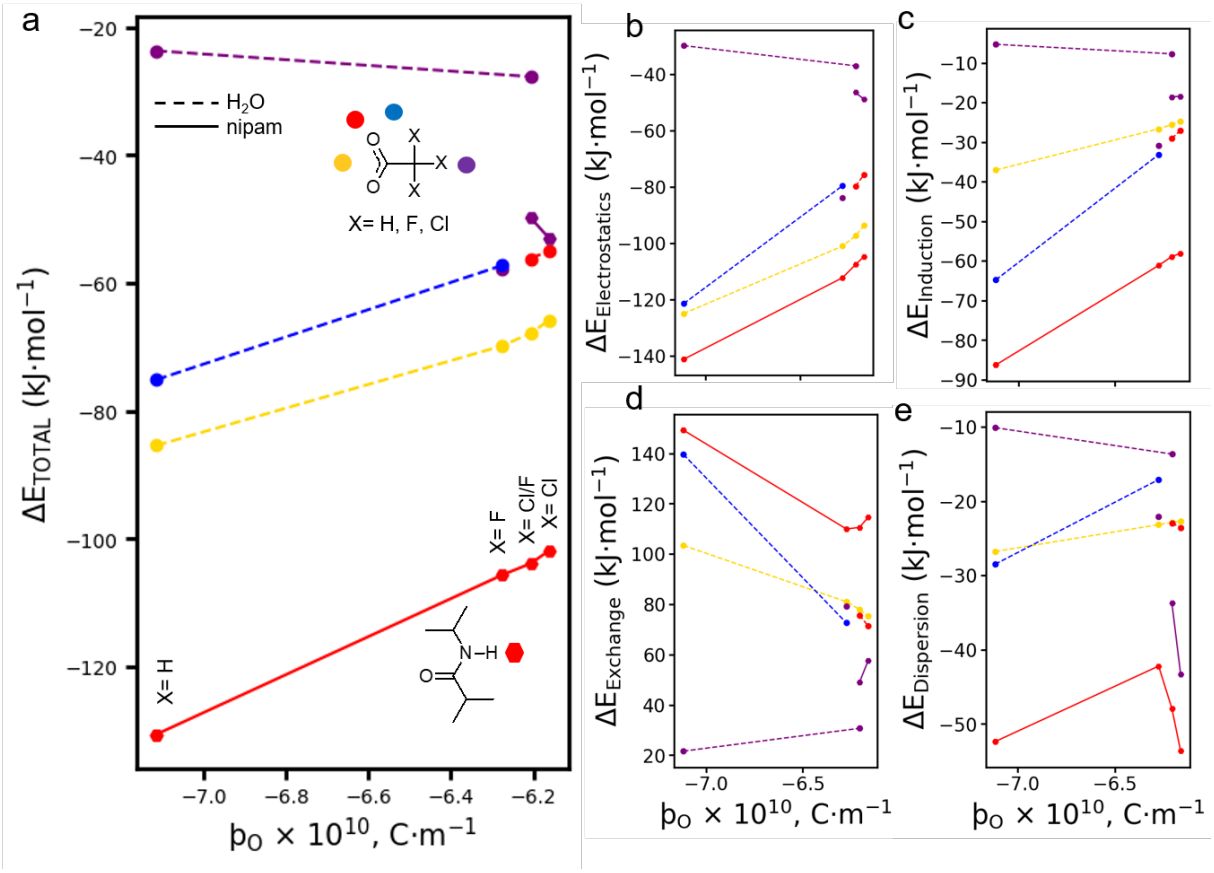

Figure S5: SAPT2+3 interaction energies between a NIPAM monomor or water molecule, and the substituted acetate ions. The total interaction energy is shown in (a) which can be composed from (b) electrostatic, (c) induction, (d) exchange, (e) dispersion components. Interactions between haloacetates and a PNIPAM fragment are shown with solid lines while interactions with a water molecule are shown with dotted lines. Colours denote different sites on the ion which can interact with either the PNIPAM fragment or water molecule. Each interaction shown here occurred at the PNIPAM fragment NH group or via a water OH group. For the total interaction strengths (a), there is a strong correlation with þ_{O^-} with the primary interact via the acetate oxygen atom. This correlation is also seen for the electrostatic (b) and induction (c) components, indicating that charge density is critical to mediating these components. The strength of exchange (d) and dispersion (e) interactions are significantly weaker and thus can be considered to not contribute to the observed specific ion effects discussed in the main manuscript.

Addressing only the total interactions (a), for both water and NIPAM, each acetate interacts predominantly via the charged oxygen atoms. These results support the hypothesis that changes in the net interactions of ions, solvent, and polymer are due to differences in the charge density of the charged oxygen groups of the acetate ions. It is worth noting these calculations are performed for isolated ion-solvent or ion-polymer pairings. As such, while these SAPT results in isolation suggest that the most charge dense unsubstituted acetate ion would bind most strongly to the PNIPAM polymer, in the multicomponent system, a more favourable interaction of the ion with the solvent would be revealed.

7 Density functional tight binding molecular dynamics simulation spatial distribution functions

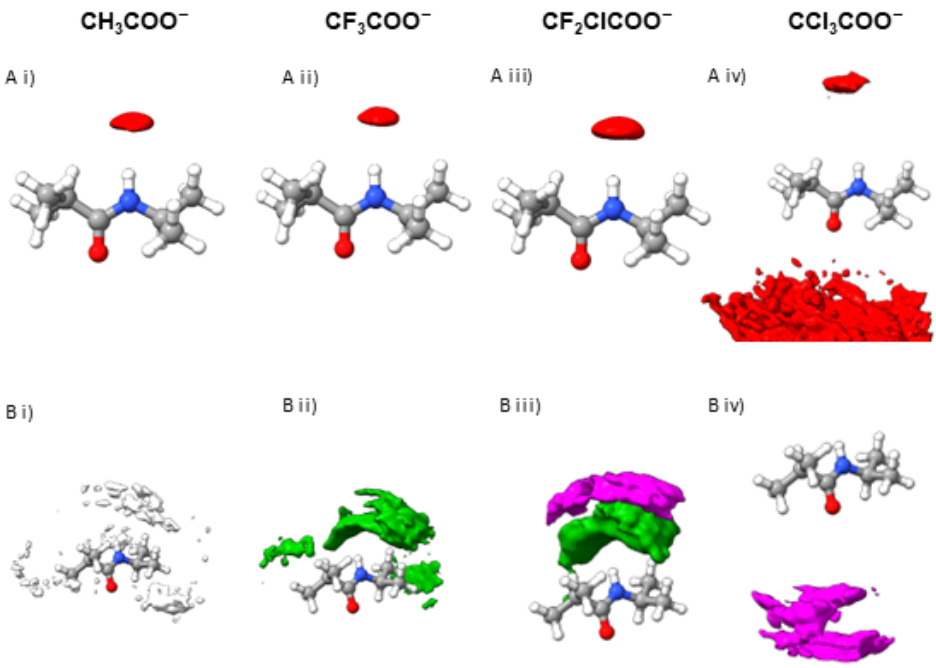

Figure S6: Spatial density function (SDF) plots for A) the charged oxygen atoms and B) the "tail" moieties of the substituted acetates around a NIPAM molecule, obtained from DFTB3-D3(BJ)/3ob-3-1 MD simulations. SDFs are shown for the i) CH_3COO^-, ii) CF_3COO^-, iii) $CClF_2COO^-$) and iv) CCl_3COO^- ions. In (B), white, green and cyan isosurfaces correspond to hydrogen, fluorine and chlorine atoms, respectively. (A) (i-iii) show that for the three ions with the largest magnitude of þ (CH_3COO^-, CF_3COO^-, $CClF_2COO^-$), unsurprisingly, the charged oxygen (red) interacts with the NIPAM residue exclusively via the amide hydrogen. For CCl_3COO^- however, the oxygen interacts with both amide and carboxylate group of the NIPAM, with the majority of oxygen density located around the latter. For CCl_3COO^- the distance of interaction between the NIPAM and the ion is greater than all the other ions. This is consistent with the strength of interaction calculated from SAPT simulations in Figure S5. (B) shows the SDFs for the interaction between the substituted acetate tail groups around the NIPAM residue. In (i), a low density of tail hydrogen (white) atoms are seen around the NIPAM residue. (ii) and (iii) show that The fluorine atom (green) are distributed most strongly around the amide moiety on the NIPAM residue. In (iii), the chlorine (magenta) atoms also interact via the NH group, as they are covalently bound to the same carbon. In (iv), chlorine atoms are localised nearer the oxygen moiety, with the distance of interaction significantly increased relative to the fluoro-substituted atoms (not-shown). This is consistent with the strength of interaction calculated from the SAPT simulations in Figure S5, and indicates that the changes in LCST of PNIPAM are likely due to changes in ion-polymer, ion-solvent, and polymer-solvent interactions dictated by differences in charge density of the charged oxygen atoms.

8 *In situ* neutron reflectometry

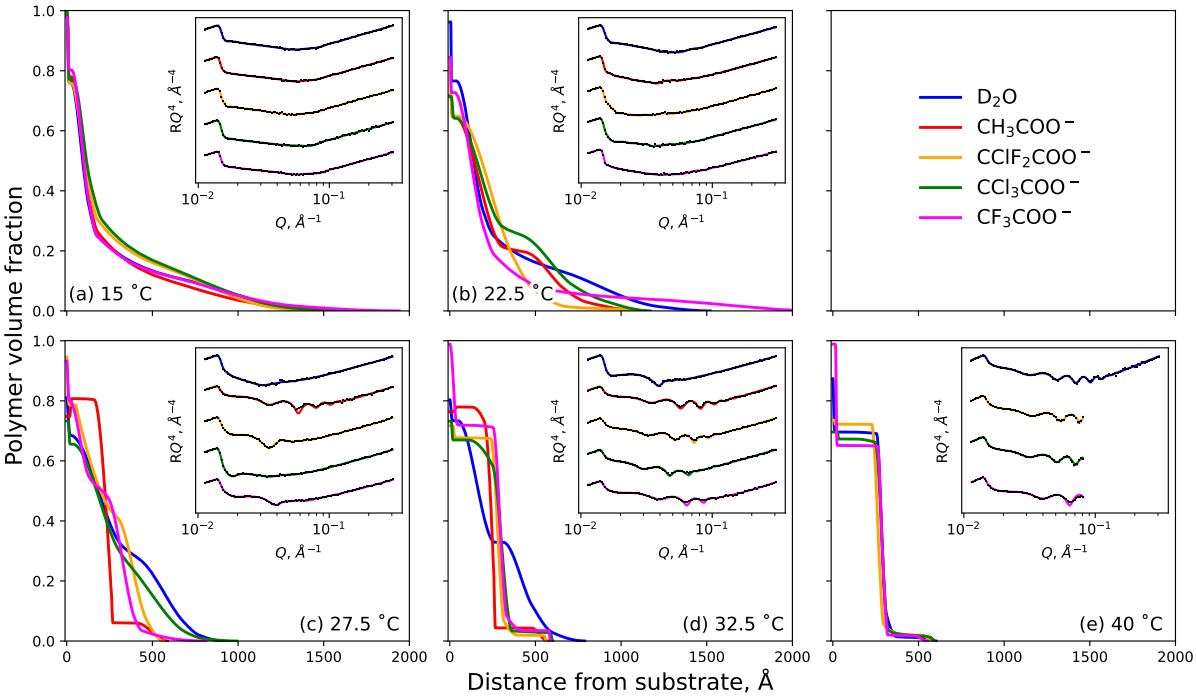

Figure S7: Neutron reflectometry derived polymer volume fraction profiles of a PNIPAM brush as a function of both electrolyte identity and temperature: (a) 15 °C, (b) 22.5 °C, (c) 27.5 °C, (d) 32.5 °C and (e) 40 °C. Insets present the reflectivity with the respective model. Note that the VF profile of the brush in acetate was acquired at 20 °C.

9 Contrast match neutron reflectometry

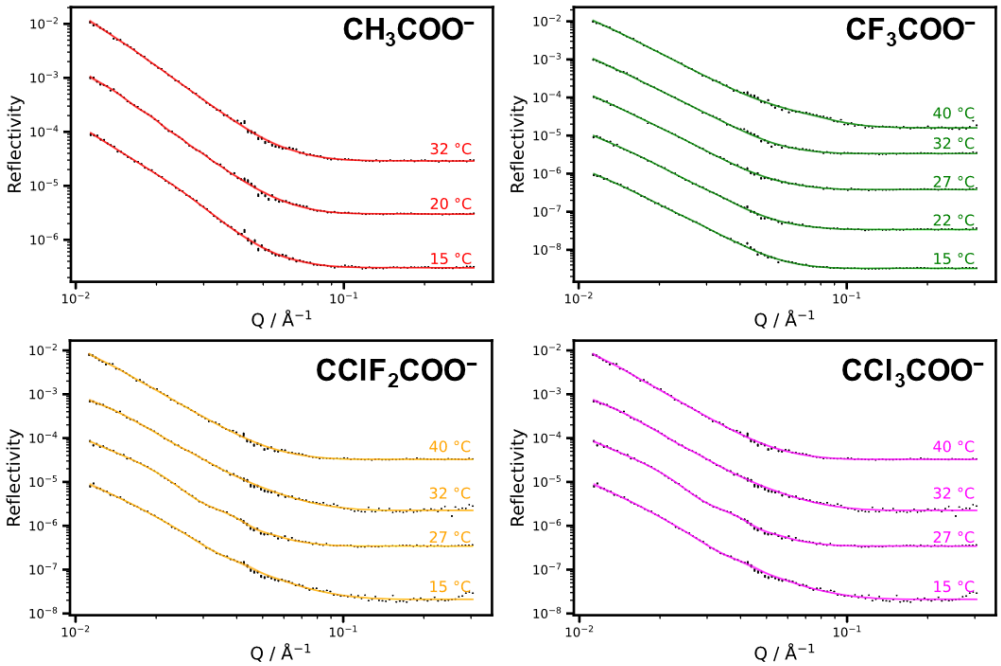

Figure S8: Experimental and modeled neutron reflectometry of a PNIPAM brush in a polymer contrast matched solution (SLD = 0.8×10^{-6} Å^{-2}). At this contrast, the reflectivity is due to scattering from salt ions, allowing for the determination of the density of salt within the brush structures

10 ^{1}H NMR of 1-Haloalkanes

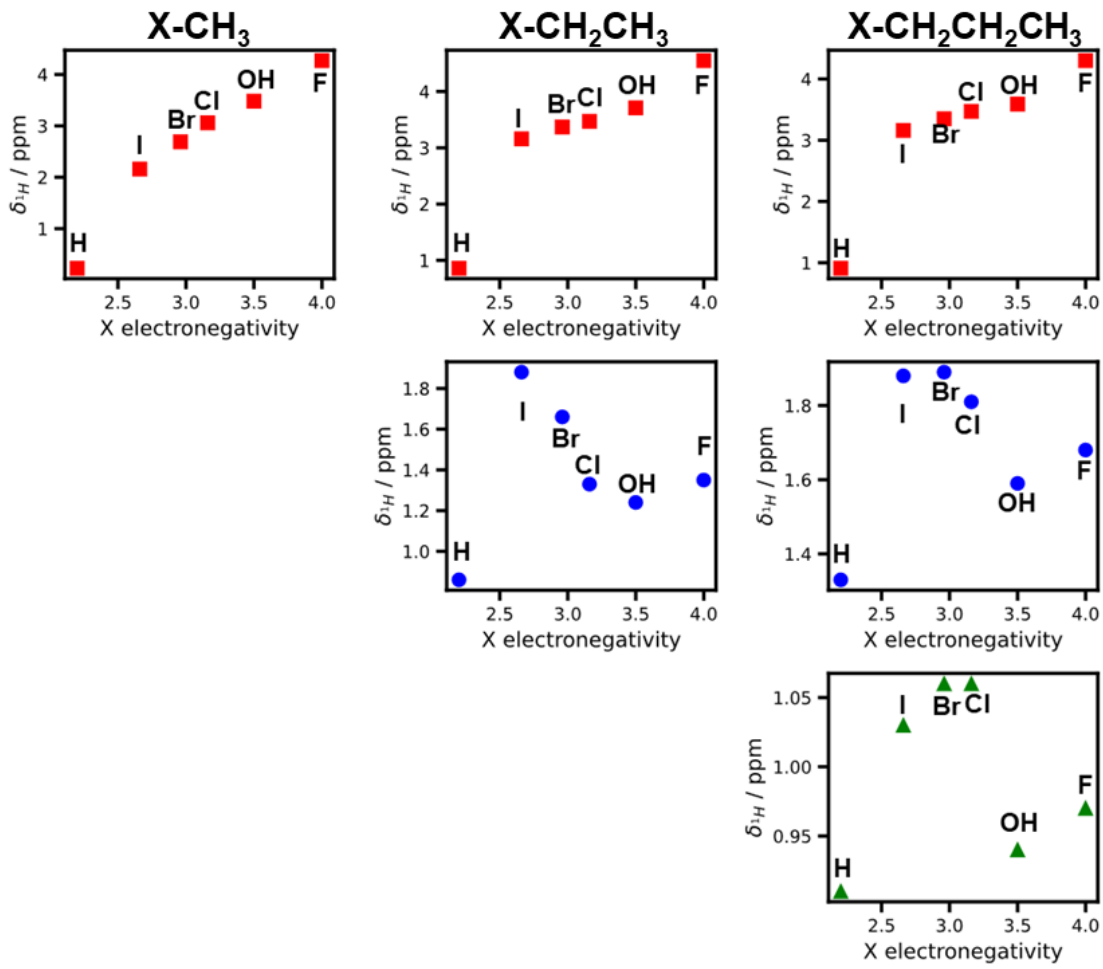

Figure S9: ^{1}H NMR chemical shifts of a number of 1-halo- and 1-alcohol alkanes ($C_n = 1$, 2, or 3) in $CDCl_3$ against the substituent electronegativity. NMR values were extracted from Pretsch et al.[38] while electronegativity values were taken from Wells.[39]

11 Bond lengths in substituted acetates

Table S2: Bond lengths in substituted acetates

Ion	**C-X$_1$** (In-plane) [Å]	**C-X$_2$** (Out-of-plane) [Å]	**C-X$_3$** (Out-of-plane) [Å]	**C-C** [Å]
CH_3COO^-	1.0877	1.0899	1.089944	1.548333
CCl_3COO^-	1.7728	1.7821	1.7824	1.622338
$CClF_2COO^-$	1.8010	1.3473	1.3473	1.577433
CF_3COO^-	1.3462	1.3535	1.3535	1.567956

References

[1] I. Auerbach, F. H. Verhoek, A. L. Henne, Kinetic Studies on the Decarboxylation of Sodium Trifluoroacetate in Ethylene Glycol, Journal of the American Chemical Society 72 (1950) 299–300. doi:10.1021/ja01157a079.

[2] M. J. Frisch, G. W. Trucks, H. B. Schlegel, G. E. Scuseria, M. A. Robb, J. R. Cheeseman, G. Scalmani, V. Barone, G. A. Petersson, H. Nakatsuji, X. Li, M. Caricato, A. V. Marenich, J. Bloino, B. G. Janesko, R. Gomperts, B. Mennucci, H. P. Hratchian, J. V. Ortiz, A. F. Izmaylov, J. L. Sonnenberg, D. Williams-Young, F. Ding, F. Lipparini, F. Egidi, J. Goings, B. Peng, A. Petrone, T. Henderson, D. Ranasinghe, V. G. Zakrzewski, J. Gao, N. Rega, G. Zheng, W. Liang, M. Hada, M. Ehara, K. Toyota, R. Fukuda, J. Hasegawa, M. Ishida, T. Nakajima, Y. Honda, O. Kitao, H. Nakai, T. Vreven, K. Throssell, J. A. J. Montgomery, J. E. Peralta, F. Ogliaro, M. J. Bearpark, J. J. Heyd, E. N. Brothers, K. N. Kudin, V. N. Staroverov, T. A. Keith, R. Kobayashi, J. Normand, K. Raghavachari, A. P. Rendell, J. C. Burant, S. S. Iyengar, J. Tomasi, M. Cossi, J. M. Millam, M. Klene, C. Adamo, R. Cammi, J. W. Ochterski, R. L. Martin, K. Morokuma, O. Farkas, J. B. Foresman, D. J. Fox, Gaussian16 revision c.01, 2016.

[3] F. Neese, Software update: The orca program system—version 5.0, WIREs Computational Molecular Science 12 (2022) e1606. URL: `https://wires.onlinelibrary.wiley.com/doi/abs/10.1002/wcms.1606`. doi:https://doi.org/10.1002/wcms.1606. `arXiv:https://wires.onlinelibrary.wiley.com/doi/`

[4] T. A. Manz, N. G. Limas, Introducing ddec6 atomic population analysis: part 1. charge partitioning theory and methodology, RSC Advances 6 (2016) 47771–47801. doi:10.1039/C6RA04656H.

[5] K. P. Gregory, E. J. Wanless, G. B. Webber, V. S. J. Craig, A. J. Page, The electrostatic origins of specific ion effects: quantifying the Hofmeister series for anions, Chemical Science 12 (2021) 15007–15015. doi:10.1039/d1sc03568a.

[6] K. P. Gregory, G. B. Webber, E. J. Wanless, A. J. Page, Decomposing Hofmeister effects on amino acid residues with symmetry adapted perturbation theory, Electronic Structure 5 (2023) 014007. doi:10.1088/2516-1075/acbe84.

[7] L. Martinez, R. Andrade, E. G. Birgin, J. M. Martínez, Packmol: A package for building initial configurations for molecular dynamics simulations, Journal of Computational Chemistry 30 (2009) 2157–2164. doi:10.1002/jcc.21224.

[8] M. Gaus, Q. Cui, M. Elstner, Dftb3: Extension of the self-consistent-charge density-functional tight-binding method (scc-dftb), Journal of Chemical Theory and Computation 7 (2012) 931–948. doi:10.1021/ct100684s.

[9] S. Grimme, S. Ehrlich, L. Goerigk, Effect of the damping function in dispersion corrected density functional theory, Journal of Computational Chemistry 32 (2011) 1456–1465. doi:10.1002/jcc.21759.

[10] M. Gaus, A. Goez, M. Elstner, Parametrization and benchmark of dftb3 for organic molecules, Journal of Chemical Theory and Computation 9 (2013) 338–354. doi:10.1021/ct300849w.

[11] R. Bukowski, W. Cencek, J. Garcia, P. Jankowski, M. Jeziorska, B. Jeziorski, S. A. Kucharski, V. F. Lotrich, M. P. Metz, A. J. Misquitta, R. Moszyński, K. Patkowski, R. Podeszwa, F. Rob, S. Rybak, K. Szalewicz, H. L. Williams, R. J. Wheatley, P. E. S. Wormer, P. S. Żuchowski, sapt2020: An *Ab Initio* program for symmetry-adapted perturbation theory calculations of intermolecular interaction energies. sequential and parallel versions, 2020.

[12] J. Garcia, R. Podeszwa, K. Szalewicz, Sapt codes for calculations of intermolecular interaction energies, Journal of Chemical Physics 152 (2020) 184109. doi:10.1063/5.0005093/1061891.

[13] T. M. Parker, L. A. Burns, R. M. Parrish, A. G. Ryno, C. D. Sherrill, Levels of symmetry adapted perturbation theory (sapt). i. efficiency and performance for interaction energies, Journal of Chemical Physics 140 (2014) 94106. doi:10.1063/1.4867135/193599.

[14] E. G. Hohenstein, C. D. Sherrill, Density fitting of intramonomer correlation effects in symmetry-adapted perturbation theory, The Journal of Chemical Physics 133 (2010) 14101. doi:10.1063/1.3451077.

[15] E. G. Hohenstein, C. D. Sherrill, Efficient evaluation of triple excitations in symmetry-adapted perturbation theory via second-order møller–plesset perturbation theory natural orbitals, The Journal of Chemical Physics 133 (2010) 104107. doi:10.1063/1.3479400.

[16] E. G. Hohenstein, C. D. Sherrill, Wavefunction methods for noncovalent interactions, WIREs Computational Molecular Science 2 (2012) 304–326. doi:10.1002/wcms.84.

[17] J. Almlöf, K. F. Jr., K. Korsell, Principles for a direct scf approach to licao–moab-initio calculations, Journal of Computational Chemistry 3 (1982) 385–399. doi:10.1002/jcc.540030314.

[18] J. H. V. Lenthe, R. Zwaans, H. J. J. V. Dam, M. F. Guest, Starting scf calculations by superposition of atomic densities, Journal of Computational Chemistry 27 (2006) 926–932. doi:10.1002/jcc.20393.

[19] J. M. Turney, A. C. Simmonett, R. M. Parrish, E. G. Hohenstein, F. A. Evangelista, J. T. Fermann, B. J. Mintz, L. A. Burns, J. J. Wilke, M. L. Abrams, N. J. Russ, M. L. Leininger, C. L. Janssen, E. T. Seidl, W. D. Allen, H. F. Schaefer, R. A. King, E. F. Valeev, C. D. Sherrill, T. D. Crawford, Psi4: an open-source ab initio electronic structure program, WIREs Computational Molecular Science 2 (2012) 556–565. doi:10.1002/wcms.93.

[20] B. Hourahine, B. Aradi, V. Blum, F. Bonafé, A. Buccheri, C. Camacho, C. Cevallos, M. Y. Deshaye, T. Dumitric, A. Dominguez, S. Ehlert, M. Elstner, T. V. D. Heide, J. Hermann, S. Irle, J. J. Kranz, C. Köhler, T. Kowalczyk, T. Kubař, I. S. Lee, V. Lutsker, R. J. Maurer, S. K. Min, I. Mitchell, C. Negre, T. A. Niehaus, A. M. Niklasson, A. J. Page, A. Pecchia, G. Penazzi, M. P. Persson, J. Řezáč, C. G. Sánchez, M. Sternberg, M. Stöhr, F. Stuckenberg, A. Tkatchenko, V. W. Yu, T. Frauenheim, Dftb+, a software package for efficient approximate density functional theory based atomistic simulations, The Journal of Chemical Physics 152 (2020) 124101. doi:10.1063/1.5143190.

[21] D. D. Johnson, Modified broyden's method for accelerating convergence in self-consistent calculations, Physical Review B 38 (1988) 12807–12813. doi:10.1103/PhysRevB.38.12807.

[22] G. J. Martyna, M. L. Klein, M. Tuckerman, Nosé–hoover chains: The canonical ensemble via continuous dynamics, The Journal of Chemical Physics 97 (1992) 2635–2643. doi:10.1063/1.463940.

[23] G. J. Martyna, M. E. Tuckerman, D. J. Tobias, M. L. Klein, Explicit reversible integrators for extended systems dynamics, Molecular Physics 87 (1996) 1117–1157. doi:10.1080/00268979600100761.

[24] M. Brehm, M. Thomas, S. Gehrke, B. Kirchner, Travis—a free analyzer for trajectories from molecular simulation, The Journal of Chemical Physics 152 (2020) 164105. doi:10.1063/5.0005078.

[25] B. A. Humphreys, E. C. Johnson, E. J. Wanless, G. B. Webber, Poly(N-isopropylacrylamide) response to salt concentration and anion identity: A brush-on-brush study, Langmuir 35 (2019) 10818–10830. doi:10.1021/acs.langmuir.9b00695.

[26] J. Genzer, In silico polymerization: Computer simulation of controlled radical polymerization in bulk and on flat surfaces, Macromolecules 39 (2006) 7157–7169. doi:10.1021/ma061155f.

[27] C. B. Gorman, R. J. Petrie, J. Genzer, Effect of substrate geometry on polymer molecular weight and polydispersity during surface-initiated polymerization, Macromolecules 41 (2008) 4856–4865. doi:10.1021/ma8004857.

[28] W. J. Brittain, S. Minko, A structural definition of polymer brushes, Journal of Polymer Science Part A: Polymer Chemistry 45 (2007) 3505–3512. doi:10.1002/pola.22180.

[29] H. Robertson, E. C. Johnson, I. J. Gresham, S. W. Prescott, A. Nelson, E. J. Wanless, G. B. Webber, Competitive specific ion effects in mixed salt solutions on a thermoresponsive polymer brush, Journal of Colloid and Interface Science 586 (2021) 292–304. doi:10.1016/j.jcis.2020.10.092.

[30] H. Robertson, I. J. Gresham, S. W. Prescott, G. B. Webber, E. J. Wanless, A. Nelson, *refellips*: A Python package for the analysis of variable angle spectroscopic ellipsometry data, SoftwareX 20 (2022) 101225. doi:10.1016/j.softx.2022.101225.

[31] H. Robertson, J. D. Willott, K. P. Gregory, E. C. Johnson, I. J. Gresham, A. R. J. Nelson, V. S. J. Craig, S. W. Prescott, R. Chapman, G. B. Webber, E. J. Wanless, From Hofmeister to hydrotrope: Effect of anion hydrocarbon chain length on a polymer brush, Journal of Colloid And Interface Science 634 (2023) 983–994. doi:10.1016/j.jcis.2022.12.114.

[32] M. James, A. Nelson, S. A. Holt, T. Saerbeck, W. A. Hamilton, F. Klose, The multipurpose time-of-flight neutron reflectometer "Platypus" at Australias OPAL reactor, Nuclear Instruments and Methods in Physics Research, Section A: Accelerators, Spectrometers, Detectors and Associated Equipment 632 (2011) 112–123. doi:10.1016/j.nima.2010.12.075.

[33] H. Robertson, A. R. J. Nelson, S. W. Prescott, G. B. Webber, E. J. Wanless, Cosolvent effects on the structure and thermoresponse of a polymer brush : PNIPAM in DMSO-water mixtures, Polymer Chemistry (2023). doi:10.1039/D2PY01487D.

[34] I. J. Gresham, T. J. Murdoch, E. C. Johnson, H. Robertson, G. B. Webber, E. J. Wanless, S. W. Prescott, A. R. J. Nelson, Quantifying the robustness of the neutron reflectometry technique for structural characterization of polymer brushes, Journal of Applied Crystallography 54 (2021) 739–750. doi:10.1107/s160057672100251x.

[35] I. J. Gresham, J. D. Willott, E. C. Johnson, P. Li, G. B. Webber, E. J. Wanless, A. R. J. Nelson, S. W. Prescott, Effect of surfactants on the thermoresponse of PNIPAM investigated in the brush geometry, Journal of Colloid and Interface Science 631 (2023) 260–271. doi:10.1016/j.jcis.2022.10.071.

[36] J.-F. F. Lutz, Ö. Akdemir, A. Hoth, Point by point comparison of two thermosensitive polymers exhibiting a similar LCST: Is the age of poly(NIPAM) over?, Journal of the American Chemical Society 128 (2006) 13046–13047. doi:10.1021/ja065324n.

[37] A. R. J. Nelson, S. W. Prescott, *refnx*: Neutron and X-ray Reflectometry Analysis in Python, Journal of Applied Crystallography 52 (2019) 193–200. doi:10.1107/S1600576718017296.

[38] E. Pretsch, P. Buhlmann, M. Badertscher, Structure Determination ofOrganic Compounds: Tables of Spectral Data, 4th ed., Springer, 2009.

[39] P. R. Wells, Group Electronegativities, Wiley, 1968, pp. 111–145. doi:10.1002/9780470171851.